Minimizing and controlling hydrogen for highly efficient $FAPbI_3$ perovskite

Yuhang Liang,[1,2] *Xiangyuan Cui*,[3,*] *Feng Li*,[2] *Catherine Stampfl*,[2] *Simon P. Ringer*,[3] *Jun Huang*,[1,*] *Rongkun Zheng*[2,*]

[1] School of Chemical and Biomolecular Engineering, The University of Sydney, NSW 2006, Australia

[2] School of Physics, The University of Sydney, NSW 2006, Australia

[3] School of Aerospace, Mechanical and Mechatronic Engineering, The University of Sydney, NSW 2006, Australia

*Xiangyuan Cui: carl.cui@sydney.edu.au

*Jun Huang: jun.huang@sydney.edu.au

*Rongkun Zheng: rongkun.zheng@sydney.edu.au

Abstract

Formamidinium lead triiodide ($FAPbI_3$) currently holds the record conversion efficiency in the single-junction perovskite solar cell. Iodine management is known to be essential to suppress defect-induced nonradiative losses in $FAPbI_3$ active layers. However, the origin of nonradiative losses and the underlying mechanism of suppressing such losses by iodine-concentration management remain unknown. Here, through first-principles simulation, we demonstrate that native point defects are not responsible for the nonradiative losses in $FAPbI_3$. Instead, hydrogen ions, which can be abundant under both iodine-rich and iodine-poor conditions in $FAPbI_3$, act as efficient nonradiative recombination centers and are proposed to be responsible for the device nonradiative losses and suppressed power conversion efficiency. Moreover, iodine-moderate synthesis conditions can favor the formation of electrically inactive molecular hydrogen, which can dramatically suppress the detrimental hydrogen ions. This work identifies the dominant nonradiative recombination centers in the widely used $FAPbI_3$ layers and rationalizes how the prevailing iodine management reduces the nonradiative losses. Minimizing the unintentional hydrogen incorporation in the perovskite is proposed to be critical for achieving high device performance.

Keywords: perovskite solar cell, $FAPbI_3$, nonradiative recombination, iodine management, first-principles calculation.

Introduction

Metal halide perovskite semiconductors have emerged as front runners for next-generation photovoltaic cells with high power conversion efficiency (PCE) and low manufacturing cost. Compared to the prototypical $MAPbI_3$ (MA = Methylammonium, CH_3NH_3), $FAPbI_3$ (FA = Formamidinium, NH_2CHNH_2) films possess the improved thermal stability and the suitable bandgap (~1.48 eV) closer to the optimal value (1.34 eV) of the Shockley-Queisser (S-Q) limit, and thus have been the most attractive candidate in perovskite solar cells[1–7]. So far, the record PCE has catapulted to over 25.8% in $FAPbI_3$-based single-junction solar cells[1], comparable or even exceeding other single-junction solar cells[8].

It is well acknowledged that iodine management by optimizing the concentration of iodine during the growth and processing of the perovskite layers is crucial for achieving high PCE values in $FAPbI_3$-based solar cells[5,9–12]. In particular, synthesizing $FAPbI_3$ films with either scarce or excess iodide ions could result in inferior solar cell performance, which is closely associated with deep-level defects and their induced nonradiative recombination losses[5,9–12]. Specifically, the experimentally observed nonradiative recombination rates in $FAPbI_3$ active layers are typically $10^6 s^{-1}$[3,10,13,14], serving as a major loss mechanism and restraining the PCE from approaching the theoretical maximum efficiency (~32%)[15]. The open-circuit voltage (V_{OC}), typically around 1.1 V for the state-of-the-art $FAPbI_3$-based solar cells[2,4,6], still lags behind the radiative limit (1.255 V from Ref.[4]). This is regarded as a direct consequence of the energy losses induced by nonradiative recombination of photogenerated charge carriers[2,4,6]. On the other hand, it has been experimentally shown that tuning the iodine content can effectively shift the electrical conductivity of halide perovskite materials, which could play an important role in the defect engineering in halide perovskites[16].

Notably, fewer first-principles defect investigations have been carried out on the $FAPbI_3$ perovskites[17] as compared with its predecessor $MAPbI_3$[18–26], whereas highly efficient perovskite solar cells are predominantly fabricated with $FAPbI_3$ active layers. This is significant because of the distinctively different defect-induced nonradiative

recombination mechanisms between $FAPbI_3$ and $MAPbI_3$. Previous reports have shown that hydrogen vacancies (V_H)[18] and iodine interstitials (I_i)[19,26] are the dominant nonradiative recombination centers in $MAPbI_3$. In contrast, in $FAPbI_3$, iodine interstitials (I_i) are actually shallow defects[27], and hydrogen vacancies of FA cations could not cause significant nonradiative loss either[18]. The origin of defect-induced nonradiative losses in $FAPbI_3$ remains unknown. Identifying and then effectively suppressing such efficiency-killing defects would further improve the performance of $FAPbI_3$-based devices. This imperatively calls for an in-depth understanding of the underlying atomistic mechanism of the nonradiative recombination in $FAPbI_3$.

In this study, by performing first-principles calculations, we reveal that native point defects are not responsible for the nonradiative losses in $FAPbI_3$; instead, electrically active hydrogen interstitials, H_i, is the dominant nonradiative recombination center with a capture coefficient on the order of $10^{-8}\mathrm{cm}^3\mathrm{s}^{-1}$ at room temperature, consistent with the experimental measurements[28]. We propose that synthesizing the $FAPbI_3$ perovskite samples under the iodide-moderate and hydrogen-poor conditions can effectively suppress the formation of detrimental H_i and thus the resultant nonradiative efficiency losses.

Results and Discussion

Figure 1 shows the phase map for the equilibrium growth condition of $FAPbI_3$ as a function of the relative chemical potential of Pb ($\Delta\mu_{Pb}$) and I ($\Delta\mu_I$). The constraints are set by three elementary phases (FA, Pb, and I) and two competing secondary phases (PbI_2 and FAI). Within the chemical potential range that stabilizes $FAPbI_3$ determined, i.e., the red region in the figure, three representative points are labeled as points A, B, and C, corresponding to iodine-poor (I-poor), moderate, and iodine-rich (I-rich) growth conditions, respectively.

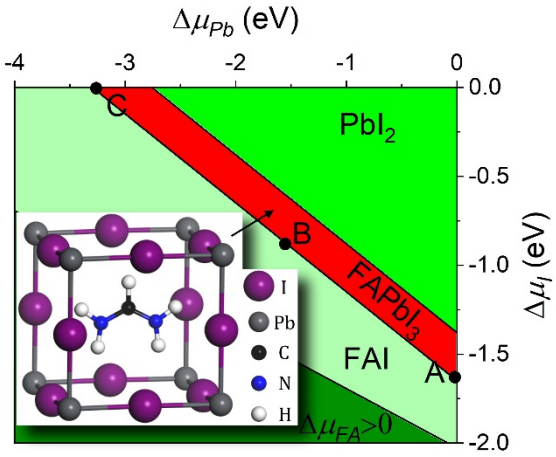

Figure 1. The phase map for thermal equilibrium growth condition of $FAPbI_3$ as a function of the relative chemical potentials $\Delta\mu_{Pb}$ and $\Delta\mu_I$. The red area shows the allowed chemical potential region where FAPbI3 is thermodynamically stable. Three different growth conditions, i.e., point A, B, and C, corresponding to the I-poor, I-moderate, and I-rich conditions, respectively, were chosen for defect formation studies.

We first systematically studied the stability of possible native point defects, including three vacancies (V_{FA}, V_{Pb}, and V_I), three interstitials (FA_i, Pb_i, and I_i), and six substitutions (FA_{Pb}, FA_I, Pb_{FA}, Pb_I, I_{FA}, and I_{Pb}), in $FAPbI_3$ with the high-level HSE+SOC+TS method. **Figure 2a-c** shows the calculated formation energies of seven lowest-energy native defects under the three representative iodine growth conditions. V_{FA} and V_{Pb} acceptors exhibit very low formation energies in $FAPbI_3$, especially under I-rich conditions. It can be seen that V_{FA} does not have a transition energy level and V_{Pb} produces a shallow acceptor level slightly (~0.06 eV) above the valence band maximum (VBM). Based on the Shockley-Read-Hall theory of recombination[29], the existence of a deep charge-state transition energy level in the bandgap is a prerequisite for a defect that acts as the nonradiative recombination center [30]. Hence, V_{FA} and V_{Pb} are not nonradiative recombination centers. Similarly, V_I and FA_i are also not nonradiative recombination centers with only +1 charge state stable in the Fermi level. The low formation energies of V_{Pb} and V_I are attributed to the strong Pb-*p* and I-*s* energetically unfavorable antibonding character of the valence band of $FAPbI_3$, resembling the *s*-*p* antibonding coupling in the prototypical $MAPbI_3$[25], which makes the Pb-I bonds easy to break and to form the defects. The low formation energy of V_{FA} can be attributed to the well-known weak van de Waals interaction between the PbI_6 inorganic framework

and the organic cations of the hybrid perovskite structure[25]. While a previous pure-PBE study suggested that I_{FA} is a deep-level defect[17], our HSE+SOC+TS calculations show that I_{FA} is a shallow defect with a high formation energy, indicating that it can only play an insignificant role. Notably, in contrast to the deep-level nature in $MAPbI_3$, I_i (I interstitials) induce a shallow acceptor level near the VBM (~0.04 eV above the VBM) in $FAPbI_3$, consistent with experimental findings[27].

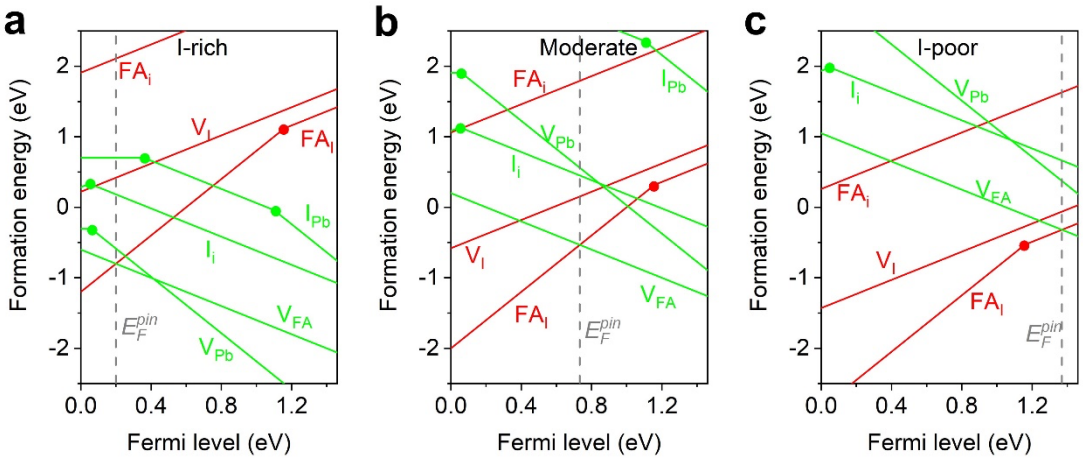

Figure 2. Formation energies of the seven low-energy intrinsic point defects in $FAPbI_3$ as a function of the Fermi level under the I-rich (a), moderate (b), and I-poor (c) growth conditions, respectively.

Significantly, both I_{Pb} and FA_I induce deep transition levels within the bandgap. The $\varepsilon(+2/+1)$ level of FA_I is located at 0.30 eV below the conduction band minimum (CBM). I_{Pb} has two transition levels within the bandgap; one is located at 1.10 eV and the other at 0.36 eV below the CBM. In principle, effective nonradiative recombination centers are often neutral and singly charged defects. The nonradiative recombination process of higher charged defects involves the capture of charge carriers by the repulsive defect, namely, hole capture by a positively charged defect or electron capture by a negatively charged center, which results in a much slower nonradiative recombination compared with that for neutral or attractive centers[29]. Similarly, a defect with multiple levels in the bandgap tends to be an inefficient nonradiative recombination center, because usually one of the levels involves a higher charged level

that has a very low capture rate, e.g., $\varepsilon(-1/-2)$ of I_{Pb}, which limits the overall capture process[31]. Indeed, our explicit calculations confirm that FA_I and I_{Pb} are not efficient nonradiative recombination centers with the very low carrier capture coefficients of $2.3 \times 10^{-20} cm^3 s^{-1}$ and $6.6 \times 10^{-14} cm^3 s^{-1}$, respectively, at room temperature (see **Figure S1**). Notably the carrier capture coefficient of I_{Pb} in $CsPbI_3$ is also on the order of $10^{-14} cm^3 s^{-1}$ at room temperature[32], which could not cause significant nonradiative recombination.

Alternatively, unintentionally incorporated impurities may play an important role. It is well established that hydrogen is a common impurity in traditional semiconductors[33] and notably, our previous studies demonstrate that it can be abundant in the lattice of hybrid Methylammonium perovskites[34]. Motivated by this, we systematically studied the energetics and nonradiative recombination properties of interstitial hydrogen defects in $FAPbI_3$. **Figure 3a** shows the formation energies of atomic H_i and molecular H_2 in $FAPbI_3$. For each species, several structural configurations in different charged states were considered. It can be seen that H_2 is electrically inactive with a thermodynamically stable neutral-charged state in $FAPbI_3$. For molecular H_2, the H-H bond length is 0.77 Å, close to 0.75 Å for free hydrogen molecules. In contrast, atomic H_i behaves as an electric-active negative-U center in $FAPbI_3$. The neutral state H_i^0 is energetically unstable compared with the positively charged H_i^+ and negatively charged H_i^- over the whole range of the Fermi level. This leads to a deep $\varepsilon(+/-)$ transition energy level, i.e., the intersection of the formation energies of H_i^+ and H_i^-, at 0.73 eV above the VBM. In a *p*-type or *n*-type $FAPbI_3$, i.e., when the Fermi level is located at the proximity of the VBM or the CBM, respectively, H_2 is unstable and tends to dissociate into hydrogen ions. In an intrinsic (low-conductivity) $FAPbI_3$, H_2 is energetically more favourable.

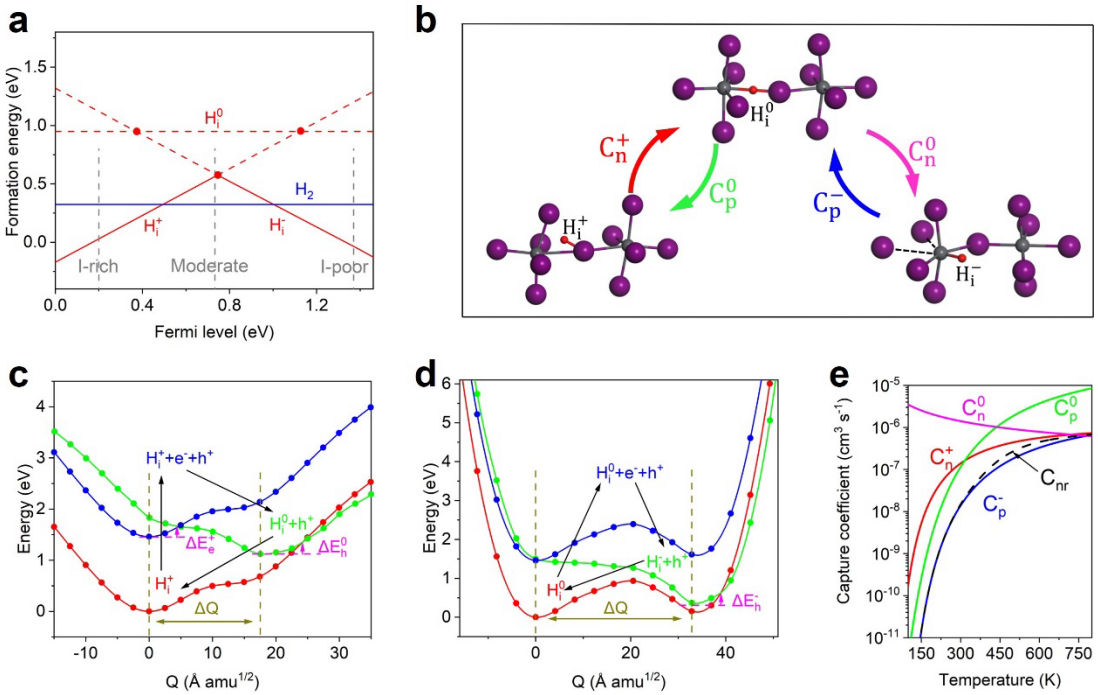

Figure 3. (a) The formation energies of hydrogen interstitials in $FAPbI_3$ as a function of the Fermi level under the H-rich conditions. The vertical dashed lines correspond to the pinned Fermi levels for the *p*-type, intrinsic, and *n*-type conductivities, respectively. (b) Local atomic configurations of H_i in the three charge states, where the notations of atoms are as those in **Figure 1** and the hydrogen interstitials are highlighted in red. The arrows and labels show the relevant carrier capture processes during the charge-state transitions. Configuration coordinate diagram for the transition of $H_i^+ \leftrightarrow H_i^0$ (c) and $H_i^0 \leftrightarrow H_i^-$ (d), respectively, as a function of a generalized configuration coordinate (Q). (e) Nonradiative capture coefficients of H_i as a function of temperature.

For such a negative-U defect, the $\varepsilon(+/-)$ transition level does not govern the nonradiative recombination even though it is deep in the bandgap, as found in the case of I_i in $MAPbI_3$[19,26], because the defect cannot capture two charge carriers of the same type, e.g., two electrons or two holes, at once. Instead, the relevant transition levels are $\varepsilon(+/0)$ (1.06 eV below the CBM) and $\varepsilon(0/-)$ (0.34 eV below the CBM), and four capture processes (two electron captures and two hole captures) are involved during the nonradiative recombination via the center[19,26].

As shown in **Figure 3b**, H_i exhibits distinctly different local atomic structures in three charge states (+, 0, and -) in $FAPbI_3$, which could be partially attributed to the ionic

character of the perovskite. During the transition between different charged states of H_i, the carrier capture processes are abbreviated as C_a^b, as shown in the labels in **Figure 3b**, where the subscript *a* specifies the carrier type ("n" for electron, and "p" for hole), and superscript *b* indicates the charge state of the defect. In the case of H_i^+, atomic hydrogen tends to bind to an I anion with a chemical bond length of 1.71 Å, compared with 1.61 Å for HI molecule. With the capture of an electron (C_n^+), H_i^+ transform into neutral-charged H_i^0. H_i^0 adopts a bond-centered configuration, in which hydrogen atom resides between the connected Pb and I atoms, with the distances of 2.08 Å and 1.88 Å to Pb and I, respectively. By further capturing another electron (C_n^0), the hydrogen ion moves to the vicinity of the Pb cation, and the local atomic configuration distorts significantly into a three-fold coordinated local PbI_6 octahedron, forming H_i^-. Conversely, the transition of $H_i^- \rightarrow H_i^0 \rightarrow H_i^+$ involves two hole-capture processes, i.e., C_p^- and C_p^0, respectively.

To quantitively determine the carrier capture coefficient of these processes, we first performed a carrier capture semiclassical analysis with the calculated configuration coordinate diagrams for the transition of $H_i^+ \leftrightarrow H_i^0$ and $H_i^0 \leftrightarrow H_i^-$. As shown in **Figure 3c**, the diagram depicts the potential energy surfaces (PES) of the charge state transition between H_i^+ and H_i^0 as a function of the generalized configuration coordinate (Q)[35,36]. The Q of each configuration is determined by its difference from a reference configuration, i.e., $Q = \sqrt{\sum_a m_a (R_a - R_{f,a})^2}$, where m_a and R_a are the mass and Cartesian coordinate of atom a; the subscript f stands for the final state of the charge transition[35]. For a H_i^+ with an electron (e^-) at the CBM and a hole (h^+) at the VBM (blue line in **Figure 3c**), it requires to overcome an energy barrier ΔE_e^+ (the intersection between potential energy surfaces of H_i^+ (blue line) and H_i^0 (green line)) to capture an electron and transition to H_i^0. Similarly, the hole capture process by H_i^0 overcomes a comparable energy barrier ΔE_h^0, as indicated by the intersection between the green line and red line in the figure, H_i^0 transitions back to H_i^+. Based on the quantum-mechanical vibronic overlap of the PES and the strength of electron-phonon coupling[35], the nonradiative electron (C_n^+) and hole (C_h^0) capture coefficients for the transition between H_i^+ and H_i^0 are $1.3 \times 10^{-7} cm^3 s^{-1}$ and $2.4 \times 10^{-8} cm^3 s^{-1}$, respectively, at room temperature, as shown in **Figure 3e**.

For the analysis of the charge state transition between H_i^0 and H_i^-, as shown in **Figure**

3d, an important feature is that the larger structural relaxation associated with the transition between H_i^0 and H_i^- results in a greater ΔQ (~ 33 Å $\mathrm{amu}^{1/2}$). The strong electron-lattice coupling leads to a large anharmonicity for the PES, which further impacts the capture barriers. It can be seen that the PES of H_i^0 exhibits a metastable minimum at the equilibrium configuration of H_i^-, which is similar to the case of I_i^0 in $MAPbI_3$[19,21]. The energy barrier of the charge-state transition determines the capture rate in principle. Notably, the transition of H_i^0 to H_i^- (C_n^0) is within the Marcus inverted region[18,37], where a very small electron-capture energy barrier (ΔE_n^0) occurs because the large anharmonicity enables that the PES of the final state (H_i^-, green line) is accidentally close to the minimum of the PES of the initial state (H_i^0, blue line) despite the large value of ΔQ. In contrast, the energy barrier (ΔE_h^-) for hole capture by H_i^- (C_p^-) is somewhat large ($\sim 0.24\ eV$) compared to other processes, implying as lower carrier capture that would be the bottleneck in the overall nonradiative recombination cycle. As expected, as shown in **Figure 3e**, the calculated nonradiative electron capture coefficient (C_n^0) for H_i^- is $1.4 \times 10^{-6} \mathrm{cm}^3 \mathrm{s}^{-1}$, much higher than that of $1.4 \times 10^{-8} \mathrm{cm}^3 \mathrm{s}^{-1}$ for the hole capture process (C_p^-), consistent with the semiclassical analysis of the capture barriers.

On the basis of balancing electron and hole capture under steady-state conditions[31], the nonradiative recombination coefficient per defect C_{nr} (C_{Tot} in Ref. 30) can be determined by $C_{nr} = \frac{C_n^0 + C_p^0}{1 + \frac{C_n^0}{C_p^-} + \frac{C_p^0}{C_n^+}}$, as indicated by the black dashed line in **Figure 3e**. At room temperature, the calculated C_{nr} of H_i is $1.50 \times 10^{-8} \mathrm{cm}^3 \mathrm{s}^{-1}$, which is in good agreement with the experimental observation of $\sim 10^{-8} \mathrm{cm}^3 \mathrm{s}^{-1}$[28], strongly indicating that H_i is an important or even dominant recombination center in $FAPbI_3$. In addition to the nonradiative recombination coefficient C_{nr}, the overall nonradiative recombination rate constant A is also related to the defect density N in the material, namely, $A = NC_{nr}$, which describes the number of nonradiative recombination events unit time (the reciprocal of nonradiative lifetime τ_{nr}).

The defect density N is critical and therefore should be suppressed by carefully managing the growth conditions. Experiments have demonstrated that iodine management plays an important role in deep-level defect engineering in the $FAPbI_3$ active layers for high-performance solar cells[5,9–12]. An iodine-moderate growth

condition is crucial for optimizing the optoelectronic performance of the perovskites, while the scarce or excess iodine conditions unavoidably lead to the formation of deep-level defects and therefore nonradiative recombination losses, resulting in inferior device performance. Here, our calculations suggest that the different iodine-content conditions can effectively affect the relative chemical potentials and consequently the defect stabilities of the perovskites. Under the I-rich conditions (**Figure 2a**), the charge neutrality of $FAPbI_3$ is largely determined by lowest-energy V_{FA} acceptor and FA_I donor, where the Fermi level is pinned approximately at the proximity of the VBM, which is a typical *p*-type conductivity. Similarly, under the I-poor conditions (**Figure 2c**), the Fermi level of $FAPbI_3$ is pinned at the proximity of the CBM, namely, an *n*-type conductivity. This is in line with experiments that the conductivity of $FAPbI_3$ can be flexibly tuned from *p*-type to *n*-type by increasing the PbI_2/FAI ratio in the precursor solution[16]. Significantly, the stabilities and densities of hydrogen interstitials are a function of the Fermi level. From **Figure 3a** and **Figure 4**, these two typical conditions indeed enhance the formation of H_i as efficient nonradiative recombination centers, which will strongly impact the carrier lifetime and power conversion. Notably, the I-rich conditions would also increase the density of shallow-level I_i that lowers the cubic-to-hexagonal transformation barrier of the $FAPbI_3$ active layer to accelerate its phase degradation, and hence, have significant repercussions on the long-term stability of perovskite solar cells[27]. Under the I-moderate conditions (**Figure 2b**), the Fermi level will be pinned around the middle of the bandgap, corresponding to an intrinsic (low) conductivity, where the formation energy of H_i increases and the electrical-inactive molecular hydrogen (H_2) serves as the dominant hydrogen interstitials under H-rich conditions (**Figure 3a** and **Figure 4**). On the other hand, the density of H_i will be reduced and hence the induced nonradiative energy loss in $FAPbI_3$ active layers will be suppressed, leading to improved device performance.

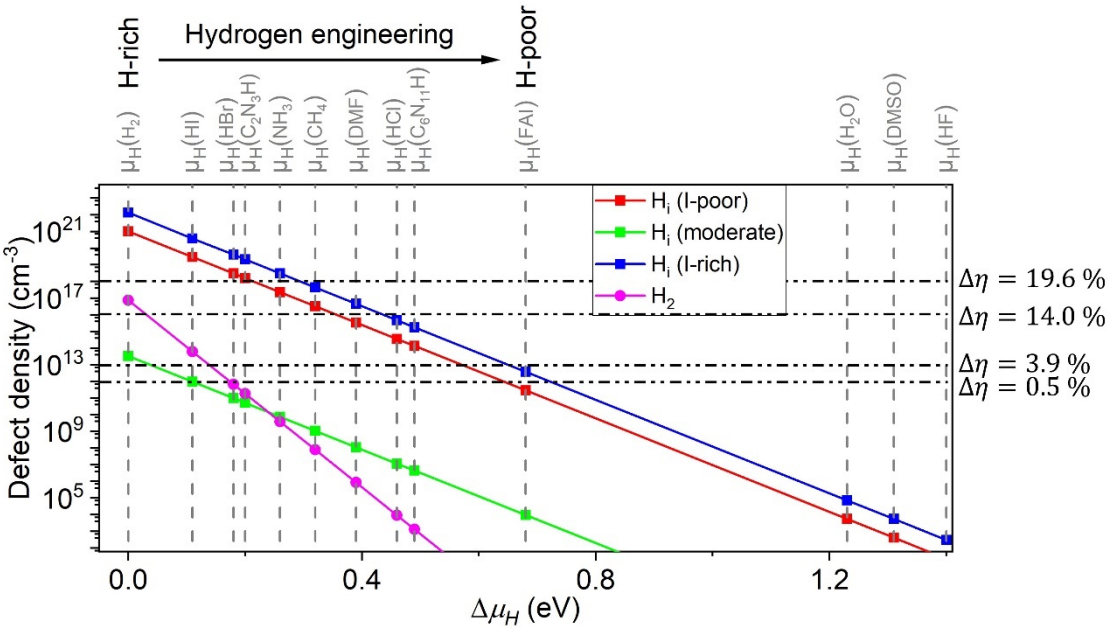

Figure 4. Calculated defect densities of H_i and H_2 at room temperature under the three representative iodine growth conditions in $FAPbI_3$, as a function of the relative chemical potential of hydrogen ($\Delta\mu_H$) in the relevant compounds (hydrogen sources). $\mu_H(H_2)$ and $\mu_H(FAI)$ correspond to the hydrogen (H)-rich and H-poor conditions, respectively. The resultant efficiency losses ($\Delta\eta$) by H_i in different defect densities are denoted.

Furthermore, we will show that, in addition to iodine management, careful control of the hydrogen environment for the preparation and operation is also important for suppressing H_i defects and further improving $FAPbI_3$-based solar cells. To reveal unintentional hydrogen incorporation under different possible hydrogen sources, we plot the defect densities of H_i and H_2 at room temperature as a function of the relative hydrogen chemical potential in **Figure 4**, under the three representative iodine growth conditions. Under the hydrogen (H)-rich conditions, it has been a common practice to set the μ_H as that in the isolated H_2 molecule. However, the H-poor condition can be simulated by considering the practical hydrogen sources. FAI, a precursor, serves as an important intrinsic hydrogen source for $FAPbI_3$, and therefore, the chemical potential of hydrogen can be around $\mu_H(FAI)$ under the H-poor conditions. As can be seen, the commonly used HI and HBr additives as well as some organic compounds, e.g., C_2N_3H and NH_3, and the DMF solvent, can be potential hydrogen sources leading to unintentional hydrogen contamination, while the water vapor, DMSO solvent, and HF can play an insignificant role. Notably, under more H-poor conditions, the electrically

inactive H_2 will be unstable with respect to dissociation into the detrimental H_i.

With the nonradiative recombination coefficient C_{nr} and defect density N, we can quantify the resultant PCE loss $\Delta\eta$ due to the nonradiative recombination by H_i. Under the detailed balance limit and ideal conditions, the light to electricity PCE is well known as the S-Q limit[15]. In the S-Q framework, the photocurrent of the solar cell is calculated as the difference between the photons absorbed and the photons flowing out the cell: $J(V) = J_P - J_{rad}(V)$, where $J_P \cong q\int_{E_g}^{\infty} \frac{2\pi}{h^3c^2} \frac{E^2}{e^{\left(\frac{E}{KT_{sun}}\right)}-1} dE$ stands for the photocurrent density, and $J_{rad}(V) \cong q\int_{E_g}^{\infty} \frac{2\pi}{h^3c^2} \frac{E^2}{e^{\left(\frac{E-qV}{KT_{cell}}\right)}-1} dE$ stands for the radiative recombination current density. q, h, K, and c are the elementary charge, Planck's constant, Boltzmann constant, and speed of light, respectively. V is the applied voltage and is equal to the splitting of the Fermi levels $qV = E_F^n - E_F^p$ under the steady condition. Therefore, the light to electricity PCE in the case of the radiative limit can be calculated by the formula $\eta = \frac{MAX(P_{out}(V))}{P_{in}} = \frac{MAX(J(V)\times V)}{P_{in}}$, where the input sun power density is given by $P_{in} = \frac{2\pi}{h^3c^2}\int_0^{\infty} \frac{E^3 dE}{e^{\left(\frac{E}{KT_{sun}}\right)}-1}$. For $FAPbI_3$ with the calculated bandgap of 1.46 eV, under AM 1.5G spectrum, the ideal power conversion efficiency (S-Q limit) can be up to $\eta\sim32.13\%$ at room temperature.

In the presence of the nonradiative recombination from H_i, the photocurrent of the solar cell will be given by: $J(V') = J_P - J_{rad}(V') - J_{nr}(V')$. The new term describes the current density loss due to the nonradiative recombination $J_{nr}(V') \cong qdAn_i e^{\left(\frac{qV'}{2KT_{cell}}\right)}$, where d, A, n_i are the thickness of the $FAPbI_3$ layer, nonradiative recombination rate constant, and intrinsic carrier concentration. We adopt the representative $d\sim300\ nm$ and $n_i\sim10^7 cm^{-3}$[38]. For the solar cell application, the nonradiative recombination is usually dominated by the defect-induced process, and the Auger recombination can play an insignificant role[39]. Therefore, the nonradiative recombination rate constant is given by the aforementioned $A = NC_{nr}$. With $P_{out}(V') = J(V') \times V'$, the resultant efficiency loss by H_i can be obtained: $\Delta\eta = \eta - \eta' = \frac{MAX\left(P_{out}(V)\right) - MAX\left(P_{out}(V')\right)}{P_{in}}$.

The estimated $\Delta\eta$ values in different H_i densities are shown in **Figure 4**. Notice even under the preferred I-moderate growth conditions, H_i can impact the device

performance with the induced efficiency loss $\Delta\eta$ being more than 4% under the H-rich conditions. This strongly suggests that H_i induced nonradiative loss can be an important loss mechanism in the $FAPbI_3$-based solar cells. To effectively suppress this detrimental effect on the device performance, the density of H_i should be controlled below the orders of $10^{12}cm^{-3}$, under which the induced $\Delta\eta$ would be less than 0.5 %. These results point to a target for hydrogen engineering to further improve the performance of the perovskite solar cells approaching their theoretical efficiency limit.

Conclusion

In summary, based on first-principles calculations, we demonstrate that native point defects are not responsible for the nonradiative losses in $FAPbI_3$. Instead, hydrogen ions can act as the dominant nonradiative recombination centers in $FAPbI_3$ with a high capture coefficient of $2.2 \times 10^{-8}\mathrm{cm}^3\mathrm{s}^{-1}$ at room temperature, in good agreement with the experimentally measured values. Both iodine-poor and iodine-rich conditions would promote the formation of detrimental H_i in $FAPbI_3$ and reduce the PCEs of the related solar cells significantly ($\Delta\eta > 10\%$). In this sense, growing the $FAPbI_3$ active layers under the I-moderate conditions and carefully controlling the hydrogen environment can effectively suppress the formation of H_i and the adverse effect on PCE. These findings are significant for possible further improvement of the $FAPbI_3$-based photovoltaic device performance.

Computational Method

First-principles calculations were performed based on density functional theory (DFT)[40] as implemented in Vienna Ab initio Simulation Package (VASP) code[41]. Projector augmented wave (PAW) pseudopotentials[42] were used with a plane-wave energy cutoff of 400 eV. The Tkatchenko-Scheffler (TS) scheme[43] was used for describing the dispersion interactions for the hybrid perovskite systems[44]. The more accurate Heyd–Scuseria–Ernzerhof hybrid functional with the mixing parameter of 0.46 was employed and the spin-orbit coupling was included (HSE+SOC). All atoms were fully relaxed until the forces on atoms are less than 0.01 eV/Å. For defect calculations in perovskite $FAPbI_3$, a $3 \times 3 \times 2$ 216-atom supercell based on the cubic

phase unit cell was employed with a Monkhorst–Pack sampling of $2 \times 2 \times 2$ k-point grid. A convergence test for a $3 \times 3 \times 3$ 324-atom supercell of $FAPbI_3$, for H_i^+, showed that the calculated formation energy difference between the 216-atom and 324-atom supercells is only 0.06 eV. Our HSE+SOC+TS calculations yield a bandgap of 1.46 eV, in good agreement with the experimental value of 1.47 eV[45]. Moreover, the optimized lattice parameter of 6.371 Å agrees well with the experimental values of 6.362 Å[45].

The defect formation energy is given by[30]:

$$\Delta H_f\left(H_i^q\right) = E\left(H_i^q\right) - E(host) - \sum n_i(\mu_i + \Delta\mu_i) + q(E_F + E(VBM) + \Delta V) \quad (1)$$

where $E\left(H_i^q\right)$ and $E(host)$ are total energies with and without defect, respectively. n_i indicates the number of defects added into the supercell. μ_i is the absolute value of the chemical potential of the defect atoms. $\Delta\mu_i$ stands for the relative value of the chemical potential, which is related to growth conditions. For the chemical potential of hydrogen (μ_H), under the H-rich conditions, it is well-defined and corresponds to the half of the total energy of an isolated H_2 molecule ($\mu_H(H_2)$). To correlate μ_H with practical H conditions, we also calculated μ_H in other relevant H-containing compounds, both possible intrinsic and extrinsic hydrogen sources, including HI, FAI ($CH(NH_2)_2I$), DMF (C_3H_7NO), DMSO (C_2H_6OS), HBr, HCl, HF, H_2O, NH_3, CH_4, C_2N_3H, and $C_6N_{11}H$, among which μ_H(FAI) was chosen as the μ_H under the H-poor conditions (FAI serves as an important intrinsic hydrogen source for the perovskite). The Fermi energy, E_F, is referenced to the VBM of $FAPbI_3$, and $E(VBM)$ represents the energy of VBM. ΔV is added for correcting the effect of periodic images of charged defects[30].

When the cubic-phase $FAPbI_3$ is stable with respect to the secondary phases of FAI and PbI_2, the chemical potential of the host should satisfy the conditions:

$$\Delta\mu_{FA} + \Delta\mu_{Pb} + 3\Delta\mu_I = \Delta H_f(FAPbI_3)$$

$$\Delta\mu_{FA} + \Delta\mu_I < \Delta H_f(FAI)$$

$$\Delta\mu_{Pb} + 2\Delta\mu_I < \Delta H_f(PbI_2)$$

where $\Delta H_f(FAPbI_3)$, $\Delta H_f(FAI)$, and $\Delta H_f(PbI_2)$ are the formation enthalpies of $MAPbI_3$, MAI, and PbI_2, respectively. To avoid the formation of elemental phases, all

the chemical potentials should be less than zero ($\Delta\mu_{FA} < 0$, $\Delta\mu_{Pb} < 0$, and $\Delta\mu_{I} < 0$).

The transition level is defined as the Fermi-level position with respect to the bulk VBM for which the formation energies of different defect charge states are equal:

$$\varepsilon(q/q') = [E(a,q) - E(a,q') - (q-q')(E(VBM) + \Delta V)]/(q-q') \quad (2)$$

The nonradiative capture coefficients are calculated using the established multiphonon emission methodology[35,46] including the effect of lattice anharmonicity[18,19,32] by solving the one-dimensional Schrodinger equation for the anharmonic potential energy surfaces. The evaluation of the electron−phonon coupling matrix elements for electron and hole capture are evaluated using the PAW results by VASP processed with the NONRAD package[35,46].

The defect concentration at thermal equilibrium can be given by[30]: $N = N_0 e^{-\frac{\Delta H}{KT}}$, where N_0 stands for the number of the available sites for defect formation per volume (cm^{-3}), ΔH is the defect formation energy, K is the Boltzmann constant, and T is temperature, which was set to room temperature.

Acknowledgments

We acknowledge the expert support provided by the Sydney Informatics Hub (SIH) team—a core research facility of the University of Sydney. This work was supported by computational resources provided by the Australian Government through Gadi under the National Computational Merit Allocation Scheme and was accessed through the SIH HPC Allocation Scheme [LE190100021]. We acknowledge partial financial supports from the Australian Research Council [DP200100940] and [DE180100167].

Conflict of Interest

The authors declare no conflict of interest.

Reference

(1) Min, H.; Lee, D. Y.; Kim, J.; Kim, G.; Lee, K. S.; Kim, J.; Paik, M. J.; Kim, Y. K.; Kim, K. S.; Kim, M. G.; Shin, T. J.; Il Seok, S. Perovskite Solar Cells with

Atomically Coherent Interlayers on SnO2 Electrodes. *Nature* **2021**, *598* (7881), 444–450. https://doi.org/10.1038/s41586-021-03964-8.

(2) Jeong, J.; Kim, M.; Seo, J.; Lu, H.; Ahlawat, P.; Mishra, A.; Yang, Y.; Hope, M. A.; Eickemeyer, F. T.; Kim, M.; Yoon, Y. J.; Choi, I. W.; Darwich, B. P.; Choi, S. J.; Jo, Y.; Lee, J. H.; Walker, B.; Zakeeruddin, S. M.; Emsley, L.; Rothlisberger, U.; Hagfeldt, A.; Kim, D. S.; Grätzel, M.; Kim, J. Y. Pseudo-Halide Anion Engineering for α-FAPbI 3 Perovskite Solar Cells. *Nature* **2021**, *592* (7854), 381–385. https://doi.org/10.1038/s41586-021-03406-5.

(3) Jeong, M.; Choi, I. W.; Go, E. M.; Cho, Y.; Kim, M.; Lee, B.; Jeong, S.; Jo, Y.; Choi, H. W.; Lee, J.; Bae, J.-H.; Kwak, S. K.; Kim, D. S.; Yang, C. Stable Perovskite Solar Cells with Efficiency Exceeding 24.8% and 0.3-V Voltage Loss. *Science* **2020**, *369* (6511), 1615–1620.

(4) Lu, H.; Liu, Y.; Ahlawat, P.; Mishra, A.; Tress, W. R.; Eickemeyer, F. T.; Yang, Y.; Fu, F.; Wang, Z.; Avalos, C. E.; Carlsen, B. I.; Agarwalla, A.; Zhang, X.; Li, X.; Zhan, Y.; Zakeeruddin, S. M.; Emsley, L.; Rothlisberger, U.; Zheng, L.; Hagfeldt, A.; Grätzel, M. Vapor-Assisted Deposition of Highly Efficient, Stable Black-Phase FAPbI3 Perovskite Solar Cells. *Science* **2020**, *370* (6512). https://doi.org/10.1126/science.abb8985.

(5) Yang, W. S.; Park, B.-W.; Jung, E. H.; Jeon, N. J.; Kim, Y. C.; Lee, D. U.; Shin, S. S.; Seo, J.; Kim, E. K.; Noh, J. H.; Seok, S. I. Iodide Management in Formamidinium-Lead-Halide–Based Perovskite Layers for Efficient Solar Cells. *Science* **2017**, *356* (6345), 1376–1379. https://doi.org/10.1126/science.aan2301.

(6) Min, H.; Kim, M.; Lee, S.-U.; Kim, H.; Kim, G.; Choi, K.; Lee, J. H.; Seok, S. I. Efficient, Stable Solar Cells by Using Inherent Bandgap of α-Phase Formamidinium Lead Iodide. *Science* **2019**, *366* (6466), 749–753. https://doi.org/10.1126/science.aay7044.

(7) Kim, G.; Min, H.; Lee, K. S.; Lee, D. Y.; Yoon, S. M.; Seok, S. I. Impact of Strain Relaxation on Performance of α-Formamidinium Lead Iodide Perovskite Solar Cells. *Science* **2020**, *370* (6512), 108–112. https://doi.org/10.1126/science.abc4417.

(8) Best Research-Cell Efficiency Chart https://www.nrel.gov/pv/assets/pdfs/best-research-cell-efficiencies-rev211011.pdf (accessed 2021 -07 -05).

(9) Kim, Y. C.; Jeon, N. J.; Noh, J. H.; Yang, W. S.; Seo, J.; Yun, J. S.; Ho-Baillie, A.; Huang, S.; Green, M. A.; Seidel, J.; Ahn, T. K.; Seok, S. I. Beneficial Effects of PbI2 Incorporated in Organo-Lead Halide Perovskite Solar Cells. *Adv. Energy Mater.* **2016**, *6* (4), 1502104. https://doi.org/10.1002/aenm.201502104.

(10) Bi, D.; Tress, W.; Dar, M. I.; Gao, P.; Luo, J.; Renevier, C.; Schenk, K.; Abate, A.; Giordano, F.; Baena, J.-P. C.; Decoppet, J.-D.; Zakeeruddin, S. M.; Nazeeruddin, M. K.; Grätzel, M.; Hagfeldt, A. Efficient Luminescent Solar Cells Based on Tailored Mixed-Cation Perovskites. *Sci. Adv.* **2016**, *2* (1), e1501170. https://doi.org/10.1126/sciadv.1501170.

(11) Park, B.; Kedem, N.; Kulbak, M.; Lee, D. Y.; Yang, W. S.; Jeon, N. J.; Seo, J.; Kim, G.; Kim, K. J.; Shin, T. J.; Hodes, G.; Cahen, D.; Seok, S. I. Understanding How Excess Lead Iodide Precursor Improves Halide Perovskite Solar Cell Performance. *Nat. Commun.* **2018**, *9* (1), 3301. https://doi.org/10.1038/s41467-018-05583-w.

(12) Deng, Y.; Xu, S.; Chen, S.; Xiao, X.; Zhao, J.; Huang, J. Defect Compensation in Formamidinium–Caesium Perovskites for Highly Efficient Solar Mini-Modules with Improved Photostability. *Nat. Energy* **2021**, *6* (6), 633–641. https://doi.org/10.1038/s41560-021-00831-8.

(13) Johnston, M. B.; Herz, L. M. Hybrid Perovskites for Photovoltaics: Charge-Carrier Recombination, Diffusion, and Radiative Efficiencies. *Acc. Chem. Res.* **2016**, *49* (1), 146–154. https://doi.org/10.1021/acs.accounts.5b00411.
(14) Rehman, W.; Milot, R. L.; Eperon, G. E.; Wehrenfennig, C.; Boland, J. L.; Snaith, H. J.; Johnston, M. B.; Herz, L. M. Charge-Carrier Dynamics and Mobilities in Formamidinium Lead Mixed-Halide Perovskites. *Adv. Mater.* **2015**, *27* (48), 7938–7944. https://doi.org/10.1002/adma.201502969.
(15) Shockley, W.; Queisser, H. J. Detailed Balance Limit of Efficiency of P-n Junction Solar Cells. *J. Appl. Phys.* **1961**, *32* (3), 510–519.
(16) Euvrard, J.; Yan, Y.; Mitzi, D. B. Electrical Doping in Halide Perovskites. *Nat Rev Mater* **2021**, *6* (6), 531–549. https://doi.org/10.1038/s41578-021-00286-z.
(17) Liu, N.; Yam, C. First-Principles Study of Intrinsic Defects in Formamidinium Lead Triiodide Perovskite Solar Cell Absorbers. *Phys. Chem. Chem. Phys.* **2018**, *20* (10), 6800–6804. https://doi.org/10.1039/C8CP00280K.
(18) Zhang, X.; Shen, J.-X.; Turiansky, M. E.; Van de Walle, C. G. Minimizing Hydrogen Vacancies to Enable Highly Efficient Hybrid Perovskites. *Nat. Mater.* **2021**, *20* (7), 971–976. https://doi.org/10.1038/s41563-021-00986-5.
(19) Zhang, X.; Turiansky, M. E.; Shen, J.-X.; Van de Walle, C. G. Iodine Interstitials as a Cause of Nonradiative Recombination in Hybrid Perovskites. *Phys. Rev. B* **2020**, *101* (14), 140101. https://doi.org/10.1103/PhysRevB.101.140101.
(20) Meggiolaro, D.; De Angelis, F. First-Principles Modeling of Defects in Lead Halide Perovskites: Best Practices and Open Issues. *ACS Energy Lett.* **2018**, *3* (9), 2206–2222. https://doi.org/10.1021/acsenergylett.8b01212.
(21) Meggiolaro, D.; Motti, S. G.; Mosconi, E.; Barker, A. J.; Ball, J.; Perini, C. A. R.; Deschler, F.; Petrozza, A.; Angelis, F. D. Iodine Chemistry Determines the Defect Tolerance of Lead-Halide Perovskites. *Energy Environ. Sci.* **2018**, *11* (3), 702–713. https://doi.org/10.1039/C8EE00124C.
(22) Wang, J.; Li, W.; Yin, W. Passivating Detrimental DX Centers in $CH_3NH_3PbI_3$ for Reducing Nonradiative Recombination and Elongating Carrier Lifetime. *Adv. Mater.* **2020**, *32* (6), 1906115. https://doi.org/10.1002/adma.201906115.
(23) Agiorgousis, M. L.; Sun, Y.-Y.; Zeng, H.; Zhang, S. Strong Covalency-Induced Recombination Centers in Perovskite Solar Cell Material $CH_3NH_3PbI_3$. *J. Am. Chem. Soc.* **2014**, *136* (41), 14570–14575. https://doi.org/10.1021/ja5079305.
(24) Yin, W.-J.; Shi, T.; Yan, Y. Unusual Defect Physics in $CH_3NH_3PbI_3$ Perovskite Solar Cell Absorber. *Appl. Phys. Lett.* **2014**, *104* (6), 063903. https://doi.org/10.1063/1.4864778.
(25) Yin, W.-J.; Yang, J.-H.; Kang, J.; Yan, Y.; Wei, S.-H. Halide Perovskite Materials for Solar Cells: A Theoretical Review. *J. Mater. Chem. A* **2015**, *3* (17), 8926–8942. https://doi.org/10.1039/C4TA05033A.
(26) Whalley, L. D.; van Gerwen, P.; Frost, J. M.; Kim, S.; Hood, S. N.; Walsh, A. Giant Huang–Rhys Factor for Electron Capture by the Iodine Intersitial in Perovskite Solar Cells. *J. Am. Chem. Soc.* **2021**, *143* (24), 9123–9128. https://doi.org/10.1021/jacs.1c03064.
(27) Tan, S.; Yavuz, I.; Weber, M. H.; Huang, T.; Chen, C.-H.; Wang, R.; Wang, H.-C.; Ko, J. H.; Nuryyeva, S.; Xue, J.; Zhao, Y.; Wei, K.-H.; Lee, J.-W.; Yang, Y. Shallow Iodine Defects Accelerate the Degradation of α-Phase Formamidinium Perovskite. *Joule* **2020**, *4* (11), 2426–2442. https://doi.org/10.1016/j.joule.2020.08.016.
(28) Dagnall, K. A.; Foley, B. J.; Cuthriell, S. A.; Alpert, M. R.; Deng, X.; Chen, A. Z.; Sun, Z.; Gupta, M. C.; Xiao, K.; Lee, S.-H.; Ma, Y.-Z.; Choi, J. J.

Relationship between the Nature of Monovalent Cations and Charge Recombination in Metal Halide Perovskites. *ACS Appl. Energy Mater.* **2020**, *3* (2), 1298–1304. https://doi.org/10.1021/acsaem.9b02310.
(29) Würfel, P. Physics of Solar Cells: From Principles to New Concepts. In *Physics of Solar Cells: From Principles to New Concepts*; Wiley-VCH Verlag: Weinheim, 2008; p 7.
(30) Kang, J.; Li, J.; Wei, S.-H. Atomic-Scale Understanding on the Physics and Control of Intrinsic Point Defects in Lead Halide Perovskites. *Applied Physics Reviews* **2021**, *8* (3), 031302. https://doi.org/10.1063/5.0052402.
(31) Alkauskas, A.; Dreyer, C. E.; Lyons, J. L.; Van de Walle, C. G. Role of Excited States in Shockley-Read-Hall Recombination in Wide-Band-Gap Semiconductors. *Phys. Rev. B* **2016**, *93* (20), 201304. https://doi.org/10.1103/PhysRevB.93.201304.
(32) Zhang, X.; Turiansky, M. E.; Van de Walle, C. G. Correctly Assessing Defect Tolerance in Halide Perovskites. *J. Phys. Chem. C* **2020**, *124* (11), 6022–6027. https://doi.org/10.1021/acs.jpcc.0c01324.
(33) Van de Walle, C. G.; Neugebauer, J. Universal Alignment of Hydrogen Levels in Semiconductors, Insulators and Solutions. *Nature* **2003**, *423* (6940), 626–628. https://doi.org/10.1038/nature01665.
(34) Liang, Y.; Cui, X.; Li, F.; Stampfl, C.; Huang, J.; Ringer, S. P.; Zheng, R. Hydrogen-Anion-Induced Carrier Recombination in MAPbI3 Perovskite Solar Cells. *J. Phys. Chem. Lett.* **2021**, *12* (43), 10677–10683. https://doi.org/10.1021/acs.jpclett.1c03061.
(35) Alkauskas, A.; Yan, Q.; Van de Walle, C. G. First-Principles Theory of Nonradiative Carrier Capture via Multiphonon Emission. *Phys. Rev. B* **2014**, *90* (7), 075202. https://doi.org/10.1103/PhysRevB.90.075202.
(36) Alkauskas, A.; McCluskey, M. D.; Van de Walle, C. G. Tutorial: Defects in Semiconductors—Combining Experiment and Theory. *J. Appl. Phys.* **2016**, *119* (18), 181101. https://doi.org/10.1063/1.4948245.
(37) Suppan, P. The Marcus Inverted Region. In *Photoinduced Electron Transfer IV*; Mattay, J., Ed.; Topics in Current Chemistry; Springer: Berlin, Heidelberg, 1992; pp 95–130. https://doi.org/10.1007/3-540-55117-4_5.
(38) Momblona, C.; Malinkiewicz, O.; Roldán-Carmona, C.; Soriano, A.; Gil-Escrig, L.; Bandiello, E.; Scheepers, M.; Edri, E.; Bolink, H. J. Efficient Methylammonium Lead Iodide Perovskite Solar Cells with Active Layers from 300 to 900 Nm. *APL Materials* **2014**, *2* (8), 081504. https://doi.org/10.1063/1.4890056.
(39) Zhang, X.; Shen, J.-X.; Van de Walle, C. G. First-Principles Simulation of Carrier Recombination Mechanisms in Halide Perovskites. *Advanced Energy Materials* **2020**, *10* (13), 1902830. https://doi.org/10.1002/aenm.201902830.
(40) Kohn, W.; Sham, L. J. Self-Consistent Equations Including Exchange and Correlation Effects. *Phys. Rev.* **1965**, *140* (4A), A1133–A1138. https://doi.org/10.1103/PhysRev.140.A1133.
(41) Kresse, G.; Furthmüller, J. Efficiency of Ab-Initio Total Energy Calculations for Metals and Semiconductors Using a Plane-Wave Basis Set. *Comput. Mater. Sci.* **1996**, *6* (1), 15–50. https://doi.org/10.1016/0927-0256(96)00008-0.
(42) Kresse, G.; Joubert, D. From Ultrasoft Pseudopotentials to the Projector Augmented-Wave Method. *Phys. Rev. B* **1999**, *59* (3), 1758–1775. https://doi.org/10.1103/PhysRevB.59.1758.
(43) Tkatchenko, A.; Scheffler, M. Accurate Molecular Van Der Waals Interactions

from Ground-State Electron Density and Free-Atom Reference Data. *Phys. Rev. Lett.* **2009**, *102* (7), 073005. https://doi.org/10.1103/PhysRevLett.102.073005.
(44) Motta, C.; El-Mellouhi, F.; Kais, S.; Tabet, N.; Alharbi, F.; Sanvito, S. Revealing the Role of Organic Cations in Hybrid Halide Perovskite CH3NH3PbI3. *Nat. Commun.* **2015**, *6* (1), 7026. https://doi.org/10.1038/ncomms8026.
(45) Weller, M. T.; Weber, O. J.; Frost, J. M.; Walsh, A. Cubic Perovskite Structure of Black Formamidinium Lead Iodide, α-[HC(NH2)2]PbI3, at 298 K. *J. Phys. Chem. Lett.* **2015**, *6* (16), 3209–3212. https://doi.org/10.1021/acs.jpclett.5b01432.
(46) Turiansky, M. E.; Alkauskas, A.; Engel, M.; Kresse, G.; Wickramaratne, D.; Shen, J.-X.; Dreyer, C. E.; Van de Walle, C. G. Nonrad: Computing Nonradiative Capture Coefficients from First Principles. *Comput. Phys. Commun.* **2021**, *267*, 108056. https://doi.org/10.1016/j.cpc.2021.108056.

TOC